Optics and Lasers in Engineering 167 (2023) 107606

Contents lists available at ScienceDirect

Optics and Lasers in Engineering

journal homepage: www.elsevier.com/locate/optlaseng

Fast single-layer reconstruction for three-dimensional structured illumination microscopy

Tianyu Zhao [a,1], Zhaojun Wang [a,1], Yanan Cai [b], Yansheng Liang [a], Shaowei Wang [a], Jingxiang Zhang [a], Tongsheng Chen [c], Ming Lei [a,*]

[a] MOE Key Laboratory for Non-equilibrium Synthesis and Modulation of Condensed Matter, School of Physics, Xi'an Jiaotong University, Xi'an, Shaanxi 710049, China
[b] College of Science, Northwest A&F University, Yangling 712100, China
[c] MOE Key Laboratory of Laser Life Science & Guangdong Provincial Key Laboratory of Laser Life Science, College of Biophotonics, South China Normal University, Guangzhou 510631, China

ARTICLE INFO

Key words:
Single-layer reconstruction
Three-dimensional super-resolution microscopy
Structured illumination microscopy
Real-time imaging
Living-cell imaging

ABSTRACT

Although three-dimensional structured illumination microscopy (3D-SIM) that enhances the spatial resolution of widefield microscope in three dimensions has been successfully commercialized as a variety of products, the low imaging speed impedes its application in fast subcellular dynamics. To adapt to fast dynamics, most 3D-SIM setups provide an option for the users by canceling the axial scanning during the acquisition, by which two-dimensional optically-sectioned, super-resolved (OS-SR) time series can be obtained with single-layer 3D-SIM data. However, the conventional reconstruction workflow implemented in the frequency domain generally takes seconds for every single reconstruction, which nullifies real-time feedback for these 3D-SIM setups. In this paper, we establish a fast single-layer reconstruction approach for 3D-SIM by extending a high-speed reconstruction framework, joint space-frequency reconstruction (JSFR), to single-layer 3D-SIM. Consequently, the reconstruction speed is improved over the conventional method, without compromising the image quality. This approach is expected to provide a useful tool for 3D-SIM microscope manufacturers and their users to achieve real-time, single-layer imaging of living cells.

1. Introduction

During the past decade, super-resolution (SR) fluorescence microscopy has found striking applications in life sciences [1–4]. Thereinto, super-resolution structured illumination microscopy (SR-SIM) provides an impressive tool for biologists owing to its unrivaled compatibility with living cell imaging [5–7]. As a unique modality of SR-SIM, three-dimensional SIM (3D-SIM) enhances the spatial resolution in all three dimensions and provides true three-dimensional imaging without missing-cone problem[8,9]. As such, 3D-SIM is highly preferred by biologists and has been widely employed in commercial super-resolution SIM systems, such as N-SIM (Nikon, Japan), DeltaVision OMX (GE Healthcare, United States), and Elyra S1 (Zeiss, German), etc.

However, 3D-SIM must collect raw SIM data at different axial positions so as to achieve increased axial resolution, i.e., for every time point, 3D-SIM requires $15 \times N$ raw images (N denotes the number of axial positions), which makes it too slow to follow subcellular dynamics in live cells. In fact, for rapid subcellular dynamics, scientists are more interested in the time series of the specimen at a certain axial position[5,10–12]. In order to achieve this goal with a 3D-SIM setup, one has to acquire and reconstruct the entire 3D-SIM stack and then pick out the two-dimensional time series at the depth of interest [13], in an extremely inefficient manner. Worse still, the 3D-SIM reconstruction implemented with three-dimensional matrixes involves a huge amount of calculations [8], making it impossible to provide real-time feedbacks of the specimens for the users.

To meet fast imaging requirements, some manufacturers of the 3D-SIMs provide a compromised solution, i.e., use single-layer 3D-SIM data at certain axial position to reconstruct an optically-sectioned, super-resolved (OS-SR) image (hereinafter termed single-layer 3D-SIM, SL3D-SIM). As such, the 3D-SIM setups can achieve fast continuous imaging of living cells at certain depth without changing the light path. For the convenience of the 3D-SIM's users, many well-known, open-source reconstruction tools, such as fairSIM [14], HiFi-SIM [15], etc., provide specific interfaces for the single-layer reconstruction of 3D-SIM data.

To date, the reconstruction algorithms for SL3D-SIM were mostly constructed on the Wiener-SIM framework designed for 2D-SIM [2,16], which termed Wiener-SL3D-SIM. Previously, the Wiener-SIM algorithm implemented in frequency domain has proven to be complex and time-consuming [17]. Comparing with Wiener-SIM, the increased number of raw images of SL3D-SIM further slows down the reconstruction of Wiener-SL3D-SIM. Typically, the computing time for a raw image size

* Corresponding author.
E-mail address: ming.lei@mail.xjtu.edu.cn (M. Lei).
[1] These authors contributed equally to this work

https://doi.org/10.1016/j.optlaseng.2023.107606
Received 17 July 2022; Received in revised form 24 March 2023; Accepted 6 April 2023
Available online 11 April 2023

of 1024 × 1024 increases to 4.5s, which nullifies real-time single-layer reconstruction for these 3D-SIM setups.

To settle this problem, we extend the recently-developed joint space-frequency reconstruction (JSFR) framework [17] to SL3D-SIM, establishing a fast reconstruction method for SL3D-SIM. Simulative and experimental results show that the developed method can improve the reconstruction speed of single-layer 3D-SIM, without sacrificing the image resolution and the sectioning capability. We expect that the fast reconstruction method will provide a useful tool for 3D-SIM microscope manufacturers and their users to construct a real-time SR microscope with instant single-layer feedback.

2. Methods

2.1. Basic principle of the conventional 3D-SIM and the Wiener-SL3D-SIM

Three-dimensional structured illumination microscopy uses illumination patterns that has both lateral and axial structures to encode the high-frequency information of the specimen into the pass-band of the microscope [8]. As a consequence, both the lateral and axial resolution of the microscope are doubled, and most importantly, settled the "missing cone" problem of the conventional widefield microscope [18]. For these two purposes, an interference field that contains five lateral spatial frequencies was specifically designed, as expressed by

$$I(\mathbf{r}) = I(\mathbf{r}_{xy}, z) = \sum_{l=-2}^{2} b_{|l|} e^{i(l\mathbf{p}_{xy}\cdot\mathbf{r}_{xy}+l\varphi)} \cdot \frac{(e^{in(l)p_z z} + e^{-in(l)p_z z})}{2} \tag{1}$$

where $b_{|l|}$ indicates the amplitude of each harmonic, $\mathbf{p}_{xy}$ and φ denote the wave vector and the phase of the lateral fundamental harmonic, p_z represents the wavenumber of the axial harmonics coupled with the ±1st-order of the lateral harmonics, $n(l)$ is enumeration variable (with $n(\pm 1) = 1$, otherwise equals to zero). This field contains five lateral harmonics in which the ±1st-order is couple with axial harmonics. Without loss of generality, we can simplify the lateral components into one dimension, yielding

$$\begin{aligned} I(x, z) &= \sum_{l=-2}^{2} b_{|l|} e^{i(lp_x x+l\varphi)} \cdot \frac{(e^{in(l)p_z z}+e^{-in(l)p_z z})}{2} \\ &= b_0 + 2b_1\cos(p_x x+\varphi)\cos(p_z z) + 2b_2\cos(2p_x x+2\varphi) \end{aligned} \tag{2}$$

Substituting the light field into the imaging model of structured illumination microscopy, the spectrum of the observed 3D image can be written as five frequency components, in which the 3D OTF of the ±1st-order component is axially extended by shifting the conventional 3D OTF to $\pm p_z$. By laterally shifting the illumination pattern and axially scanning the focal plane through the specimen, the five components can be separated by solving a 5 × 5 equation sets. Eventually, super-resolved image in three dimensions can be recovered by the Wiener-based protocol developed by Gustaffson [8]. Since the above 3D images and the 3D OTF of the 3D-SIM are all denoted by three-dimensional matrixes, the 3D-SIM reconstruction involves a huge amount of calculations.

As the 3D-SIM requires equidistant axial scanning throughout the specimen, its imaging speed is generally insufficient to follow sub-second subcellular dynamics. As a complement, SL3D-SIM cancels the axial scanning at a price of a compromised axial resolution. Without requiring the axial scanning, the light field in Eq. (2) can be simplified to be a one-dimension structured field at the focal plane

$$\begin{aligned} I(x) &= b_0 + 2b_1\cos(p_x x+\varphi) + 2b_2\cos(2p_x x+2\varphi) \\ &= I_0\left[1 + m_1\cos(px+\varphi) + m_2\cos(2px+2\varphi)\right] \end{aligned} \tag{3}$$

where p_x is denoted by p for sake of brevity, m_1 and m_2 indicate the modulation depth of the first-order and second-order harmonics. As such, the five frequency components of the specimen can be separated, shifted, and superimposed in a similar way as conventional 2D-SIM, yielding a SR-SIM image with enhanced lateral resolution [2,17]. Besides, to settle the "missing cone" problem of the widefield microscope, the OTF attenuation strategy is generally employed by multiplying the shifted spectrum components with an empirical attenuation function, thereby enabling the OS-SR image to be obtained [17,19]. Hereinafter, we term the Wiener-based reconstruction method modified for SL3D-SIM the Wiener-SL3D-SIM method. As the principle and workflow of Wiener-SL3D-SIM are nearly the same to that of the conventional 2D-SIM, no more detailed description about it will be provided for sake of brevity.

2.2. Single-layer 3D-SIM reconstruction in real space

In this section, we will derive a basic reconstruction scheme for SL3D-SIM in real space. This reconstruction workflow is equivalent to a Wiener-free reconstruction protocol, where the spectrum components are overlapped without OTF compensation, OTF attenuation and the final deconvolution, The Wiener-free reconstruction protocol is the basis of the new reconstruction method.

For linear structured illumination microscopy, the detected intensity distribution at the sensor plane can be described by the following equation

$$D(\mathbf{r}) = [O(\mathbf{r}) \cdot I(\mathbf{r})] \otimes H(\mathbf{r}) \tag{4}$$

where $O(\mathbf{r})$ denotes the spatial distribution of fluorophore in the labeled specimen, $I(\mathbf{r})$ represents the intensity distribution of the excitation field, and $H(\mathbf{r})$ depicts the point spread function of the microscope. The symbol ⊗ represents the convolution operation. By shifting the excitation field with a lateral movement, the above equation can be revised as

$$D_i(\mathbf{r}) = [O(\mathbf{r}) \cdot I(\mathbf{r}-\mathbf{r}'_i)] \otimes H(\mathbf{r}) \tag{5}$$

where $\boldsymbol{r}'_i$ represents the lateral shift of the field. Without loss of generality, we only consider the structured light field in one dimension. Therefore, the vector r can be replaced by a scalar x:

$$D_i(x) = \int O(x'')I(x''-x'_i)H(x-x'')dx'' \tag{6}$$

Assuming there exists $c_i(x)$ ($i = 1, 2, 3, 4, 5$) that makes the following equation always true for any $O(x)$ and $H(x)$, the effective PSF of the system can be obtained by multiplying the wide-field PSF $H(x)$ with a modulation function $1 + \cos(px) + \cos(2px)$:

$$\begin{aligned} I_{\mathrm{SR-SIM}}(x) &= c_1(x)D_1(x)+c_2(x)D_2(x)+c_3(x)D_3(x)+c_4(x)D_4(x)+c_5(x)D_5(x) \\ &= O(x) \otimes \{[1+\cos(px)+\cos(2px)] \cdot H(x)\} \end{aligned} \tag{7}$$

Obviously, the FWHM of the effective PSF turns out to be about half of the wide-field PSF. By substituting Eqs. (5) and (6) into the above formula, the precondition for the establishment of Eq. (7) can be simplified to

$$\begin{aligned} & I_0\sum_{i=1}^{5} c_i(x)[1 + m_1\cos(px''+\varphi_0-px'_i) + m_2\cos(2px''+2\varphi_0-2px'_i)] \\ &= 1+\cos(px-px'')+\cos(2px-2px'') \\ &= 1+\cos[(px+\varphi_0)-(px''+\varphi_0)]+\cos[(2px+2\varphi_0)-(2px''+2\varphi_0)] \end{aligned} \tag{8}$$

By rewriting both sides of this equation as a function of $\cos(px''+\varphi_0)$, $\cos(2px''+2\varphi_0)$, $\sin(px''+\varphi_0)$, and $\sin(2px''+2\varphi_0)$, the above equation can be rewritten as

$$\begin{aligned} & I_0\sum_{i=1}^{5} c_i(x) + [m_1 I_0\sum_{i=1}^{5} c_i(x)\cos(px'_i)]\cos(px''+\varphi_0) \\ & +[m_1 I_0\sum_{i=1}^{5} c_i(x)\sin(px'_i)]\sin(px''+\varphi_0) \\ & +[m_2 I_0\sum_{i=1}^{5} c_i(x)\cos(2px'_i)]\cos(2px''+2\varphi_0) \\ & +[m_2 I_0\sum_{i=1}^{5} c_i(x)\sin(2px'_i)]\sin(2px''+2\varphi_0) \end{aligned}$$

$$= 1 + \cos(px + \varphi_0)\cos(px'' + \varphi_0) + \sin(px + \varphi_0)\sin(px'' + \varphi_0) + \cos(2px + 2\varphi_0)\cos(2px'' + 2\varphi_0) + \sin(2px + 2\varphi_0)\sin(2px'' + 2\varphi_0) \quad (9)$$

According to the orthogonality of $\cos(px'' + \varphi_0), \cos(2px'' + 2\varphi_0), \sin(px'' + \varphi_0)$, and $\sin(2px'' + 2\varphi_0)$, $c_i(x)$ $(i = 1, 2, 3, 4, 5)$ must satisfy the following relations, if we want the above formula to be always true for any x and x"

$$\sum_{i=1}^{5} c_i(x) = \frac{1}{I_0} \quad (10)$$

$$\sum_{i=1}^{5} c_i(x)\cos(\omega x'_i) = \frac{1}{m_1 I_0}\cos(px + \varphi_0) \quad (11)$$

$$\sum_{i=1}^{5} c_i(x)\sin(\omega x'_i) = \frac{1}{m_1 I_0}\sin(px + \varphi_0) \quad (12)$$

$$\sum_{i=1}^{5} c_i(x)\cos(2\omega x'_i) = \frac{1}{m_2 I_0}\cos(2px + 2\varphi_0) \quad (13)$$

$$\sum_{i=1}^{5} c_i(x)\sin(2\omega x'_i) = \frac{1}{m_2 I_0}\sin(2px + 2\varphi_0) \quad (14)$$

Assuming the phase shift to be $\omega x'_i \in \{0, \Delta\varphi_1, \Delta\varphi_2, \Delta\varphi_3, \Delta\varphi_4\}$, the above relations can be rewritten as follows

$$\begin{pmatrix} 1 & 1 & 1 & 1 & 1 \\ 1 & \cos\Delta\varphi_1 & \cos\Delta\varphi_2 & \cos\Delta\varphi_3 & \cos\Delta\varphi_4 \\ 0 & \sin\Delta\varphi_1 & \sin\Delta\varphi_2 & \sin\Delta\varphi_3 & \sin\Delta\varphi_4 \\ 1 & \cos 2\Delta\varphi_1 & \cos 2\Delta\varphi_2 & \cos 2\Delta\varphi_3 & \cos 2\Delta\varphi_4 \\ 0 & \sin 2\Delta\varphi_1 & \sin 2\Delta\varphi_2 & \sin 2\Delta\varphi_3 & \sin 2\Delta\varphi_4 \end{pmatrix} \begin{pmatrix} c_1(x) \\ c_2(x) \\ c_3(x) \\ c_4(x) \\ c_5(x) \end{pmatrix} = \begin{pmatrix} \frac{1}{I_0} \\ \frac{1}{m_1 I_0}\cos(px + \varphi_0) \\ \frac{1}{m_1 I_0}\sin(px + \varphi_0) \\ \frac{1}{m_2 I_0}\cos(2px + 2\varphi_0) \\ \frac{1}{m_2 I_0}\sin(2px + 2\varphi_0) \end{pmatrix} \quad (15)$$

Let

$$\mathbf{S} = \begin{pmatrix} 1 & 1 & 1 & 1 & 1 \\ 1 & \cos\Delta\varphi_1 & \cos\Delta\varphi_2 & \cos\Delta\varphi_3 & \cos\Delta\varphi_4 \\ 0 & \sin\Delta\varphi_1 & \sin\Delta\varphi_2 & \sin\Delta\varphi_3 & \sin\Delta\varphi_4 \\ 1 & \cos 2\Delta\varphi_1 & \cos 2\Delta\varphi_2 & \cos 2\Delta\varphi_3 & \cos 2\Delta\varphi_4 \\ 0 & \sin 2\Delta\varphi_1 & \sin 2\Delta\varphi_2 & \sin 2\Delta\varphi_3 & \sin 2\Delta\varphi_4 \end{pmatrix} \quad (16)$$

we can always get $c_i(x)$ $(i = 1, 2, 3, 4, 5)$ with the following formulae, as long as the above matrix $\mathbf{S}$ is full rank

$$\begin{pmatrix} c_1(x) \\ c_2(x) \\ c_3(x) \\ c_4(x) \\ c_5(x) \end{pmatrix} = \mathbf{S}^{-1} \begin{pmatrix} \frac{1}{I_0} \\ \frac{1}{m_1 I_0}\cos(px + \varphi_0) \\ \frac{1}{m_1 I_0}\sin(px + \varphi_0) \\ \frac{1}{m_2 I_0}\cos(2px + 2\varphi_0) \\ \frac{1}{m_2 I_0}\sin(2px + 2\varphi_0) \end{pmatrix} \quad (17)$$

The above formulas are the general expressions of $c_i(x)$ $(i = 1, 2, 3, 4, 5)$. Specifically, if the phase shifts are set as $\{0, \alpha, 2\alpha, 3\alpha, 4\alpha\}$, the formulas can be simplified to:

$$\begin{pmatrix} c_1(x) \\ c_2(x) \\ c_3(x) \\ c_4(x) \\ c_5(x) \end{pmatrix} = \begin{pmatrix} 1 & 1 & 1 & 1 & 1 \\ 1 & \cos\alpha & \cos 2\alpha & \cos 3\alpha & \cos 4\alpha \\ 0 & \sin\alpha & \sin 2\alpha & \sin 3\alpha & \sin 4\alpha \\ 1 & \cos 2\alpha & \cos 4\alpha & \cos 6\alpha & \cos 8\alpha \\ 0 & \sin 2\alpha & \sin 4\alpha & \sin 6\alpha & \sin 8\alpha \end{pmatrix}^{-1} \begin{pmatrix} \frac{1}{I_0} \\ \frac{1}{m_1 I_0}\cos(px + \varphi_0) \\ \frac{1}{m_1 I_0}\sin(px + \varphi_0) \\ \frac{1}{m_2 I_0}\cos(2px + 2\varphi_0) \\ \frac{1}{m_2 I_0}\sin(2px + 2\varphi_0) \end{pmatrix} \quad (18)$$

Similar to the 2D-SIM case, $c_i(x)$ is fully determined by the illumination parameters, including the initial phase, pattern frequency, phase shifts, and the modulation depths. With fixed illumination parameters, we can precompute these coefficient functions in advance reuse them for consecutive SR frames, which greatly reduces the calculations for each reconstruction. Consequently, a super-resolved image of the sample can be obtained by simply multiplying the five raw images with the coefficient functions and summing all the products up, as described in Eq. (7). The above reconstruction scheme is the spatial domain reconstruction (SDR) workflow for single-layer 3D-SIM.

2.3. Joint space-frequency reconstruction of SL3D-SIM

As demonstrated in Ref. [17], the above SDR workflow is equivalent to a Wiener-free reconstruction protocol, where the spectrum components are overlapped without OTF compensation. In addition, as the out-of-focus background is not taken into consideration, the SR image obtained with above method will suffer from strong background and significant honeycomb artifact when imaging thick specimens.

To settle these issues, we extend the connection of the SDR method and the conventional Wiener-SIM in Ref. [17] to single-layer 3D-SIM. Similarly, the lacking OTF compensation and OTF attenuation in conventional method can also be simplified to a preset filtering operation on the initial raw images, that is,

$$D'_{d,i}(\mathbf{r}) = D_{d,i}(\mathbf{r}) \otimes \mathcal{F}^{-1}\left\{[1 - a(\mathbf{k})] \cdot \tilde{H}^*(\mathbf{k})\right\} \quad (19)$$

where $D_{d,i}(\mathbf{r})$ denotes the acquired raw images in dth direction (d = 1,2,3), i indicates the step index of phase-shifting (i = 1,2,3,4,5), $\tilde{H}^*(\mathbf{k})$ is the complex conjugate of the optical transfer function of the system, [1-a(**k**)] represents the attenuation function to suppress the fluorescence background and the honeycomb artifacts in Wiener-SIM, in which $a(\mathbf{k})$ is defined as a Gaussian function,

$$a(\mathbf{k}) = a_{\text{att}} e^{-\frac{\mathbf{k}^2}{2k_\sigma^2}} \quad (20)$$

where a_{att} is the attenuation amplitude and k_σ is the attenuation width, both of which are empirically adjusted parameters.

As such, we can obtain an optically-sectioned, super-resolution image by directly substituting the filtered raw images $D'_{d,i}(\mathbf{r})$ into Eq. (7) and completing the Wiener deconvolution. In other words, the reconstruction result equivalent to that of single layer 3D-SIM can be obtained via the following equation

$$I_{\text{JSFR-SL3D-SIM}}(\mathbf{r}) = \mathcal{F}^{-1}\left\{\frac{\mathcal{F}[\sum_{d=1}^{3}\sum_{i=1}^{5} c_{d,i}(\mathbf{r}) D'_{d,i}(\mathbf{r})]}{\sum_{d=1}^{3}\left\{\sum_{l=-2}^{2}\left[1 - a(\mathbf{k} - l\mathbf{k}_d)\right]\left|\tilde{H}(\mathbf{k} - l\mathbf{k}_d)\right|^2\right\} + \alpha^2}\right\} \quad (21)$$

where α denotes the empirical parameter for Wiener deconvolution.

Therefore, we can summarize the joint space-frequency reconstruction workflow for single-layer 3D-SIM (JSFR-SL3D-SIM) as one preparation procedure and three main steps. In the preparation procedure, the illumination parameters are first estimated by the cross-correlation method [8]. Besides, the coefficient functions are calculated for later use. In the main reconstruction, fifteen raw images are firstly filtered by the attenuated OTF $[1 - a(\mathbf{k})]\tilde{H}^*(\mathbf{k})$, as indicated by Eq. (19). Subsequently, the fifteen filtered raw images are multiplied with the precalculated coefficient functions, resulting in nine intermediate images. Eventually, we can obtain the super-resolved, optically-sectioned image by summing the intermediate images up and completing the Wiener deconvolution, as described in Eq. (21). The resulting workflow greatly releases the computing burden of Wiener-SL3D-SIM because majority of the basic procedures in the original method, including the Fourier transform, band separation, band shifting, and band superposition are mostly simplified to point multiplication and summation in real space (Fig. 2).

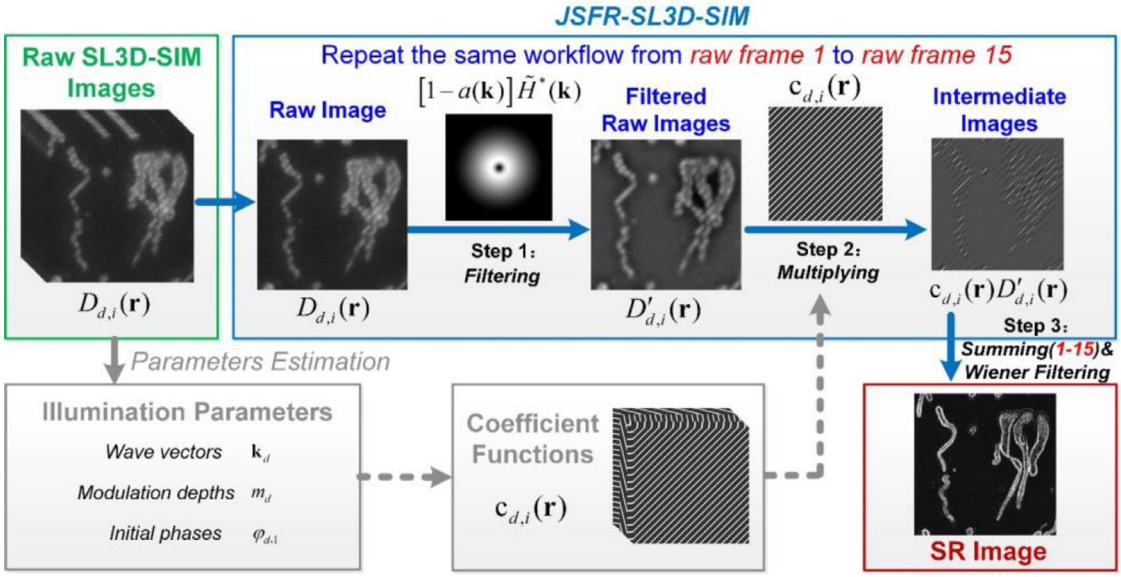

Fig. 1. The diagram to illustrate the workflow of the JSFR-SL3D-SIM. Before the main reconstruction, the illumination parameters are obtained with parameter estimation algorithms, with which the coefficient functions for each raw image can be directly obtained with Eq. (17). In the main reconstruction procedures, each raw image is initially filtered by the attenuated OTF. Afterward, fifteen intermediate images are obtained by respectively multiplying the filtered raw images with the corresponding coefficients. Eventually, the final OS-SR image can be reconstructed by summing the intermediate images up and completing the final Wiener deconvolution, as described by Eq. (21).

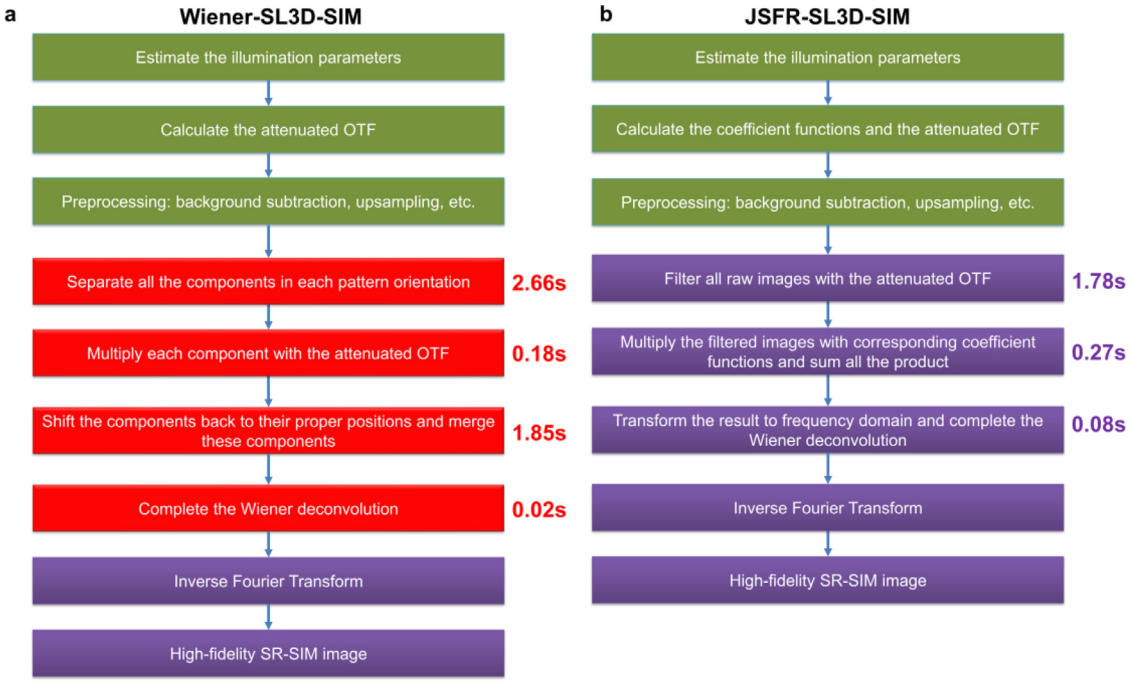

Fig. 2. Comparison of the computing burden of the conventional Wiener-SL3D-SIM (a) and the developed JSFR-SL3D-SIM (b). To provide an intuitionistic impression of the source of computing burden, the execution time of each main procedure in the two algorithms is listed on the right-hand side of the diagrams, which was tested in CPU (Intel Core i7–9700 K) with a raw image size of 1024 × 1024.

3. Results

3.1. Reconstruction speed of JSFR-SL3D-SIM

The JSFR-SL3D-SIM scheme with a simplified workflow is anticipated to significantly improve the low reconstruction speed of Wiener-SL3D-SIM. As a verification, we compared the execution time of JSFR-SL3D-SIM and Wiener-SL3D-SIM as a function of image size. Results show that when executed in central processing unit (CPU), JSFR-SL3D-SIM reconstructs an SR-image 2-fold faster than Wiener-SL3D-SIM (Table 1). In addition, we also covert the code of both algorithms to the GPU-accelerated format. Aided by a high-end commercial graphic card (NVIDIA GeForce RTX 3080ti), the environment conversion respectively results in a 23- to 50-fold speed increase for JSFR-SL3D-SIM and a 10- to 16-fold increase for Wiener-SL3D-SIM, as depicted in Table 1. In the GPU environment, JSFR-SL3D-SIM is able to reconstruct images nearly 6-fold faster than Wiener-SL3D-SIM, and this speed is nearly 90-fold faster than Wiener-SL3D-SIM executed in the CPU environment. Criti-

Table 1
The JSFR-SL3D-SIM assisted by GPU provides a near-instant reconstruction of all image sizes.

Input image size	Output image size	Collection time(ms)[a]	Execution time[b] of JSFR-SL3D-SIM (ms)		Execution time of Wiener-SL3D-SIM (ms)	
			CPU	GPU	CPU	GPU
1024 × 1024	2048 × 2048	75.0	2134.5 ± 23.5 (2.1)[c]	41.8 ± 6.3 (6.7)	4556.0 ± 28.1	282.4 ± 9.0
512 × 512	1024 × 1024	37.5	420.9 ± 7.3 (2.4)	11.1 ± 4.0 (7.6)	1002.5 ± 38.1	85.0 ± 2.9
256 × 256	512 × 512	18.8	114.5 ± 7.5 (2.5)	5.0 ± 0.2 (5.4)	285.4 ± 21.0	26.8 ± 0.6

[a] The collection time for single layer raw data under the maximal framerate of a widely-used sCMOS camera (Flash4, Hamamatsu, Japan). As each SL3D-SIM image requires fifteen raw frames, the total collection time is obtained by multiplying the collection time of single raw image with fifteen.

[b] The execution time are measured from 2000 separate processing events of each image, with the times averaged. The comparison of the reconstruction speed was done using MATLAB (R2020a, Math Works Inc.). The reconstruction codes for Wiener-SL3D-SIM and JSFR-SL3D-SIM (both CPU and the GPU versions) were executed on a personal computer (Intel Core i7–9700K@3.6 GHz, DRR4 3200 MHz 32GB, NVIDIA GeForce RTX 3080ti, Samsung 860 EVO 500GB SSD) running Windows 10.

[c] The values in parentheses are the fold increase in processing speed of the JSFR-SL3D-SIM algorithm relative to Wiener-SL3D-SIM in the same environment.

cally, the reconstruction speed using Wiener-SL3D-SIM is always slower than the acquisition time, even in the GPU-accelerated environment. In contrast, JSFR-SL3D-SIM reconstructs images more rapidly than it takes to collect them, which is much more suitable for real-time imaging than the conventional Wiener-SL3D-SIM.

3.2. JSFR-SL3D-SIM performs as good as wiener-SL3D-SIM in spatial resolution and sectioning capability

To test the performance of the algorithm in improving the spatial resolution and optical sectioning capability, we first simulated the image formation and reconstruction process of a synthetic object, which is composed of a conical spiral curve sliced into one hundred layers. The depth of the 3D spiral curve gradually increases from 0 μm at the central point to 6 μm at the periphery. The raw SIM images are generated by the general forward imaging model for SR-SIM in Eq. (4), in which the three-dimensional PSF of the system was calculated with the expression provided by Hanser et al. [20]. To obtain the full view of the sample, we recovered the full widefield stack, the Wiener-SL3D-SIM stack, and the JSFR-SL3D-SIM stack. As illustrated by the selected images from the stacks in Fig. 3d–g, both the wide-field images are deteriorated by the out-of-focus background due to the missing-cone problem. In contrast, by employing OTF compensation and OTF attenuation, the JSFR-SIM removes the out-of-focus information and significantly improves the lateral resolution, which is identical to that of the conventional Wiener-SL3D-SIM. Despite the simulative data used, the SR images obtained with SDR-SL3D-SIM suffer from some artifacts due to the out-of-focus background as shown in the intensity profiles of Fig. 3e. Also, the superior image quality of the MIP image in Fig. 3h–k demonstrates the excellent performance of the JSFR-SIM method in observing thick samples.

In addition, we examined the image quality of the JSFR-SL3D-SIM approach with an open-access experimental dataset (20,210,420_H9C2-dTag_GAL_37C_1520_sim-fasterer_017.tif) [13,21], in which the cells were adapted to galactose and their outer mitochondrial membranes were labeled by EGFP. The selected dataset was collected with a DeltaVision OMX Blaze v4 (GE Healthcare) 3D-SIM system equipped with an oil-immersion objective (60X/1.42NA, Olympus). With an axial scanning interval of 0.125 μm, the cell distributed in 1 μm was optically sliced into nine layers, and the time-lapse series of the volumetric region was collected with a time interval of 1 s. The full 3D-SIM images recovered with the vender-manufactured software GE SoftWoRx can also be downloaded in the DataverseNO website [21].

We first assess the spatial resolution and optical sectioning capability of JSFR-SL3D-SIM by recovering the first volume of the dataset, as shown in Fig. 4. By comparing the maximum-intensity-projection (MIP) images and the depth-color-coded (DCC) images recovered by varying methods, we found the overall image quality obtained SL3D-SIM methods including the fairSIM, the Wiener-SL3D-SIM, and the JSFR-SL3D-SIM has no significant degradation comparing with the traditional full 3D-SIM reconstruction. As displayed by the magnified-views of the recovered volumes at varying depths (Fig. 4c–e), the lateral spatial resolution of JSFR-SL3D-SIM are identical to that of 3D-SIM, fairSIM and Wiener-SL3D-SIM. As expected, the JSFR-SL3D-SIM, as well as fairSIM and Wiener-SL3D-SIM, presents weaker sectioning capability than the full 3D-SIM reconstruction (yellow arrows, Fig. 4d). However, the SL3D-SIM methods including JSFR-SL3D-SIM, fairSIM, and Wiener-SL3D-SIM avoid the crosstalk between the first slice and the last slice (blue arrow, Fig. 4c), which are superior to that of the full 3D-SIM reconstruction. In summary, the reconstruction quality of JSFR-SL3D-SIM is identical to that of fairSIM and Wiener-SL3D-SIM, and critically, the SR images reconstructed with the three SL3D-SIM methods are comparable to that of the same layer in full 3D-SIM reconstruction, although there is no 2-fold axial resolution improvement.

Further, we recovered the entire time-lapse series with one hundred time points respectively by pseudo-widefield, Wiener-SL3D-SIM and JSFR-SL3D-SIM, as shown in Fig. 5. The outer mitochondrial membranes which remain fuzzy in the pseudo-widefield images can be distinguished in the Wiener-SL3D-SIM and JSFR-SL3D-SIM images. With the close-up views, the mitochondrial tubulation events (Fig. 5b-5g) can be identified via the images recovered with JSFR-SL3D-SIM, as well as Wiener-SL3D-SIM. For example, a tubulation event was readily visible between 23 and 48s, as shown in Fig. 5c-5d. Besides, a “double-kiss-and-run” event can be clearly observed between 34 and 74s, as illustrated in Fig. 5f-5g. Here, a mitochondrion extended a tubulation tip nearly 2.6 μm, contacted another mitochondrion (respectively at t = 51s and t = 66s), then immediately retreated in the opposite direction.

4. Discussion

As verified by simulative results and open-source experimental datasets, the developed JSFR-SL3D-SIM method improves the reconstruction speed of single-layer 3D-SIM, without compromising any of the optical sectioning capability or the spatial resolution of the conventional SL3D-SIM method. As such, most post-processing programs for SR-SIM, such as fairSIM[14], OpenSIM[22], or SIMToolbox[23] can easily benefit from its fast reconstruction speed, which is particularly useful for the SR reconstruction of time-lapse movies. For example, the open-source dataset used in Fig. 5 contains 13,500 raw images (5 phase shifts × 3 orientations × 9 slices × 100 time points) with 256 × 256 pixels. In convention, it takes 257 and 24s for Wiener-SL3D-SIM to obtain the entire OS-SR stack in CPU and GPU environments. In contrast, the developed JSFR-SL3D-SIM method only requires 4.5s in GPU, which greatly saves the waiting time for daily reconstructions.

With the help of GPU acceleration, the JSFR-SL3D-SIM method reduces the single-layer reconstruction time to several milliseconds, which is even shorter than the acquisition time of the raw images with all frequently-used image sizes (see Table 1). Integrated with

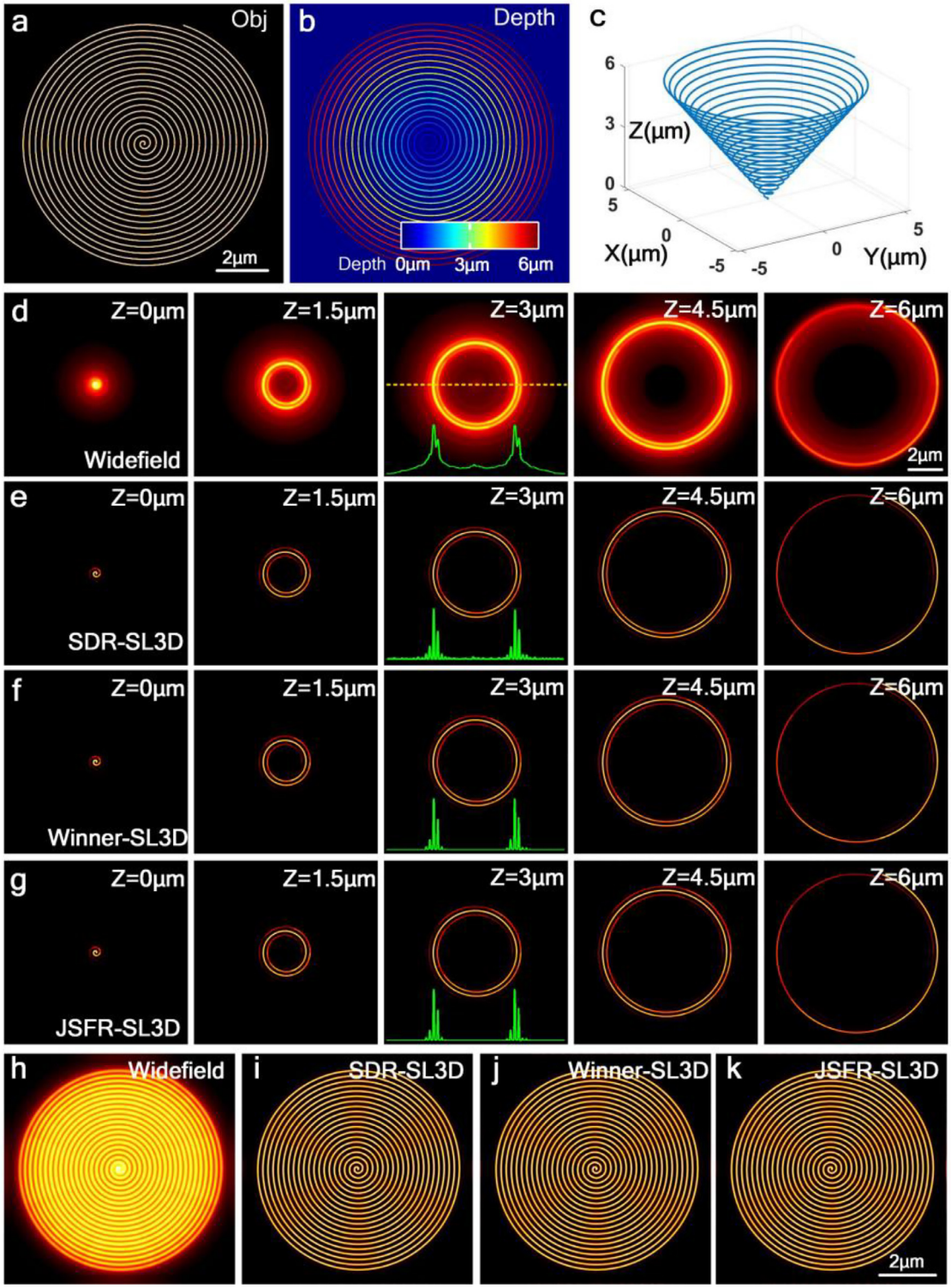

Fig. 3. Simulative result verifies the performance of JSFR-SL3D-SIM for thick samples. (a) The simulative object is composed of a conical spiral curve, which was divided into one hundred layers. (b) The depth of the 3D spiral curve gradually increases from 0 μm at the central point to 6 μm at the boundary. (c) The three-dimensional plot of the conical spiral curve. To compare the performance the full view of the sample, we recovered the widefield stack and the JSFR-SL3D-SIM stack of the one hundred layers of the simulative object. (d)-(f) are respectively five images of the specimen at equidistant focal planes in the widefield, the SDR-SL3D-SIM, Wiener-SL3D-SIM, and the JSFR-SL3D-SIM image stacks. The embedded curves in the third column of (d)-(g) are the intensity profiles of the images along the yellow-dashed line in (d). (h)-(k) are respectively the maximum-intensity-projection (MIP) images of the simulative object imaged using widefield, SDR-SL3D-SIM, Wiener-SL3D-SIM, and JSFR-SL3D-SIM. The numerical aperture of the objective, the wavelength of light, and the pixel size at the focal plane in the simulation were respectively set as 1.49, 0.52 μm, and 21.6 nm.

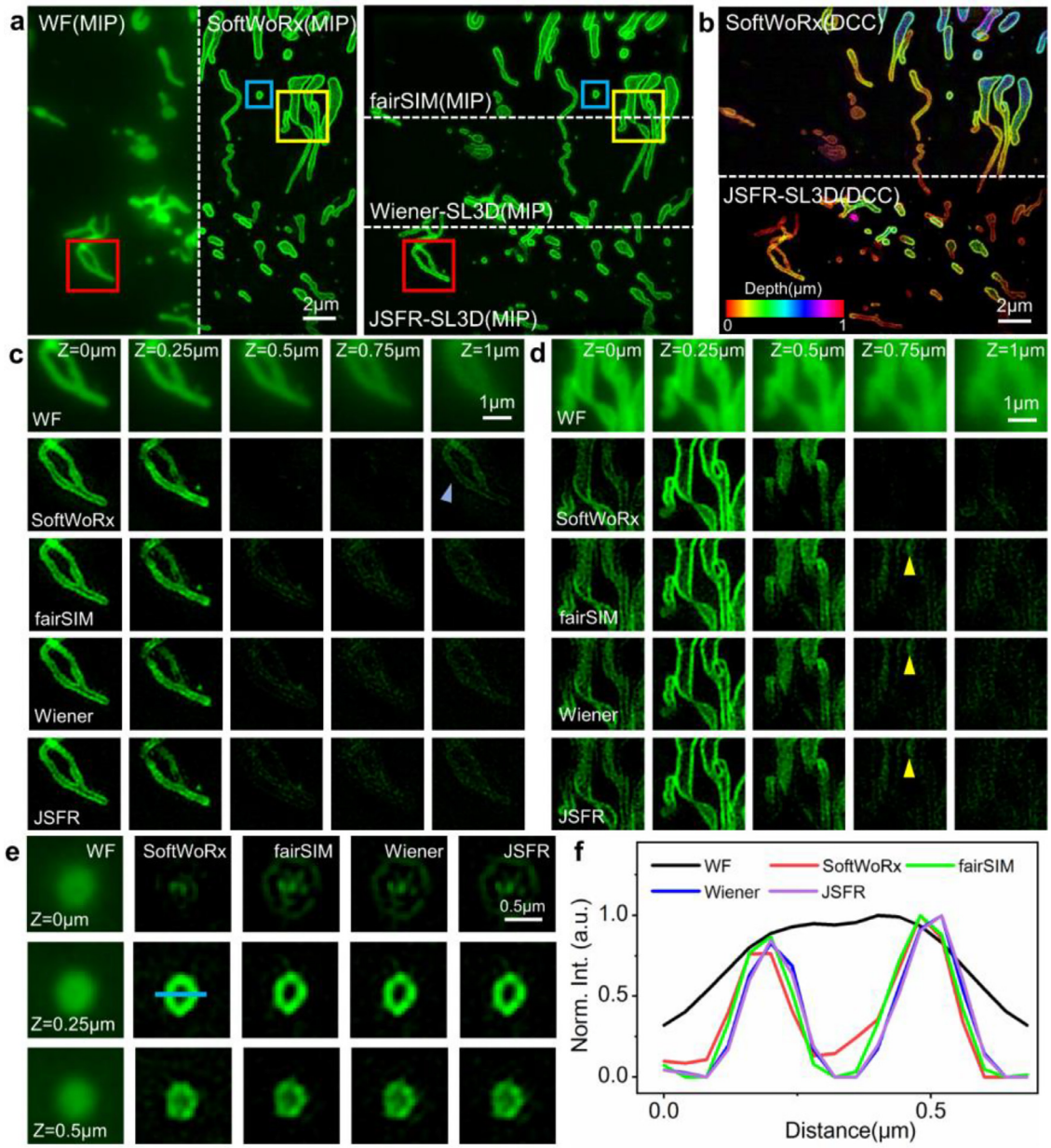

Fig. 4. JSFR-SL3D-SIM enables superior single-layer reconstruction on 3D-SIM raw data. The open-source raw 3D-SIM data used here (the first time point of 20,210,420_H9C2-dTag_GAL_37C_1520_sim-fasterer_017.tif) was downloaded from the DataverseNO website [http://dx.doi.org/10.18710/PDCLAS], which imaged the outer mitochondrial membranes in the rat cardiomyoblast cell-line H9c2. (a) The maximum-intensity-projection (MIP) images of the outer mitochondrial membranes obtained separately using the widefield microscopy, 3D-SIM and JSFR-SL3D-SIM. The negative intensities in the original 3D-SIM images are set to zero for visualization purpose. The MIP images for each were calculated by projecting the voxels with maximum intensity along the axial direction. (b) The depth-color-coded (DCC) image of the specimen recovered with the JSFR-SL3D-SIM. (c)-(d) are respectively widefield images, 3D-SIM images recovered with SoftWoRx, and OS-SR-SIM images reconstructed with fairSIM, Wiener-SL3D-SIM, and JSFR-SL3D-SIM at five equidistant focal planes in the red- and yellow-boxed regions of (a). (e) The close-up views of the widefield images, the 3D-SIM images, and the OS-SR-SIM images at three equidistant focal planes in the blue-boxed regions of (a). (f) The intensity profiles of mitochondria along the blue solid line in the close-up views in (e) for different reconstruction algorithms. The maximal intensities of the magnified views are simultaneously adjusted to present the details.

high-efficiency controlling time-sequence of available 3D-SIM setups, this method allows real-time single-layer reconstruction and result display for 3D-SIM, providing a promising tool to achieve real-time, high-resolution preview of the specimen in 3D-SIM setups. In other words, the microscopists who own 3D-SIM setups can get instant feedback from the specimen under the help of the JSFR-SL3D-SIM method, just like using a conventional widefield/confocal microscope. Such coherent and natural workflow brought by JSFR-SL3D-SIM will dramatically reduce their workload and improve their work efficiency.

As a universal improvement for SR-SIM, this method can be easily extended to other techniques to increase both reconstruction speed and image fidelity. Deep learning algorithms have made significant progress in different areas[24,25]. It is expected to combine our algorithm and deep learning methods and improve the performance. Recently, computational imaging techniques are effective ways to ease the constraints of optical architectures and improve the image quality. It is worth watching to combine JSFR-SL3D-SIM with other technologies such as incoherent imaging[26] and single-pixel imaging[27] for more possibilities.

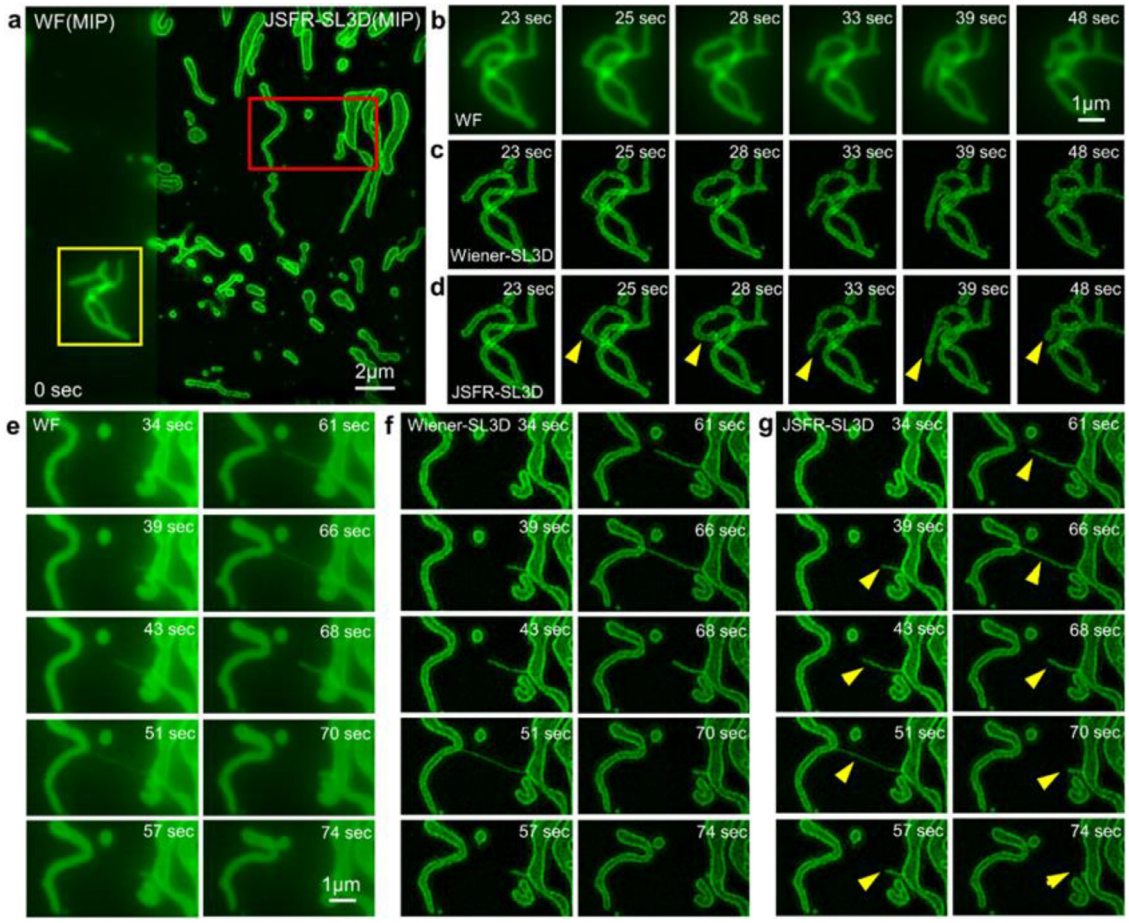

Fig. 5. JSFR-SL3D-SIM enables rapid single-layer reconstruction of subcellular dynamics. (a) The maximum-intensity-projection (MIP) images of the first volume of the time series, which were recovered using pseudo-widefield microscopy, Wiener-SL3D-SIM and JSFR-SL3D-SIM, respectively. The yellow and red solid boxed regions in (a) are magnified and presented by the time-lapse montages (b)-(d) and (e)-(g). Yellow arrows in (d) and (g) indicate the mitochondrial tubulation events.

5. Conclusion

In summary, we developed a rapid, single-layer reconstruction scheme for 3D-SIM by extending the joint space and frequency reconstruction method to the single-layer 3D-SIM, termed JSFR-SL3D-SIM. With this scheme, SR images are reconstructed faster than conventional algorithms. Importantly, the enhanced reconstruction speed does not come at the expense of the optical sectioning capability or the spatial resolution of the SR images, as verified by simulative results and open-source experimental datasets. With JSFR-SL3D-SIM, the single-layer reconstruction speed of 3D-SIM can easily be reduced to millisecond scales, thereby providing a promising tool to achieve real-time, high-resolution preview of live cells. This breakthrough will help the 3D-SIM manufacturers and the owners of 3D-SIM setups to construct real-time, living-cell, SR microscopes, greatly improve the work efficiency of their users.

Funding

This work was supported by the Natural Science Foundation of China (NSFC) (62135003, 62005208, 62205267, 12204380), National Key Research and Development Program of China (2022YFF0712500) ,Innovation Capability Support Program of Shaanxi (Program No. 2021TD-57), and Natural Science Basic Research Program of Shaanxi (2022JZ-34, 2020JQ-072, 2022JQ-069); We appreciate Standard Imaging (Beijing) Biotechnology Co. Ltd for assistance with sample preparation.

Disclosures

Zhaojun Wang and Ming Lei hold a patent (patent no. ZL202110985056.7) on JSFR-SIM. All other authors declare they have no competing interests.

Declaration of Competing Interest

The authors declare that they have no known competing financial interests or personal relationships that could have appeared to influence the work reported in this paper.

CRediT authorship contribution statement

Tianyu Zhao: Conceptualization, Investigation. **Zhaojun Wang:** Software, Investigation, Writing – original draft. **Yanan Cai:** Data curation, Investigation. **Yansheng Liang:** Software, Investigation, Visualization. **Shaowei Wang:** Writing – review & editing. **Jingxiang Zhang:** Software, Investigation, Visualization. **Tongsheng Chen:** Writing – review & editing. **Ming Lei:** Funding acquisition, Supervision, Writing – review & editing.

Data availability

Data will be made available on request.

References

[1] Klar TA, et al. Subdiffraction resolution in far-field fluorescence microscopy[J]. Opt Lett 1999;24(14):954–6.
[2] Gustafsson MG. Surpassing the lateral resolution limit by a factor of two using structured illumination microscopy[J]. J Microsc 2000;198(2):82–7.
[3] Betzig E, et al. Imaging intracellular fluorescent proteins at nanometer resolution[J]. Science 2006;313(5793):1642–5.
[4] Rust MJ, et al. Sub-diffraction-limit imaging by stochastic optical reconstruction microscopy (STORM)[J]. Nat Methods 2006;3(10):793–6.
[5] Huang X, et al. Fast, long-term, super-resolution imaging with Hessian structured illumination microscopy[J]. Nat Biotechnol 2018;36(5):451–9.
[6] Guo Y, et al. Visualizing intracellular organelle and cytoskeletal interactions at nanoscale resolution on millisecond timescales[J]. Cell 2018;175(5):1430–42.
[7] Zhanghao K, et al. Super-resolution imaging of fluorescent dipoles via polarized structured illumination microscopy[J]. Nat Commun 2019;10:4694.
[8] Gustafsson MG, et al. Three-dimensional resolution doubling in wide-field fluorescence microscopy by structured illumination[J]. Biophys J 2008;94(12):4957–70.
[9] Shao L, et al. Super-resolution 3D microscopy of live whole cells using structured illumination[J]. Nat Methods 2011;8(12):1044–6.
[10] Yang Z, et al. Cyclooctatetraene-conjugated cyanine mitochondrial probes minimize phototoxicity in fluorescence and nanoscopic imaging[J]. Chem Sci 2020;11(32):8506–16.
[11] Yang X, et al. Mitochondrial dynamics quantitatively revealed by STED nanoscopy with an enhanced squaraine variant probe[J]. Nat Commun 2020;11(1):1–9.
[12] Lin R, et al. Subcellular three-dimensional imaging deep through multicellular thick samples by structured illumination microscopy and adaptive optics[J]. Nat Commun 2021;12(1):1–14.
[13] Opstad IS, et al. Three-dimensional structured illumination microscopy data of mitochondria and lysosomes in cardiomyoblasts under normal and galactose-adapted conditions[J]. Sci Data 2022;9(1):1–7.
[14] Müller M, et al. Open-source image reconstruction of super-resolution structured illumination microscopy data in ImageJ[J]. Nat Commun 2016;7(1):1–6.
[15] Wen G, et al. High-fidelity structured illumination microscopy by point-spread-function engineering[J]. Light Sci Appl 2021;10(1):1–12.
[16] Heintzmann R, et al. Laterally modulated excitation microscopy: improvement of resolution by using a diffraction grating[C]. Optical biopsies and microscopic techniques, iii. Sweden: Stockholm; 1999. p. 185–96.
[17] Wang Z, et al. High-speed image reconstruction for optically sectioned, super-resolution structured illumination microscopy[J]. Adv Photonics 2022;4(2):026003.
[18] Sheppard C, et al. Three-dimensional transfer functions for high-aperture systems[J]. J Opt Soc Amer A 1994;11(2):593–8.
[19] O'holleran K, et al. Optimized approaches for optical sectioning and resolution enhancement in 2D structured illumination microscopy[J]. Biomed Opt Express 2014;5(8):2580–90.
[20] Hanser BM, et al. Phase retrieval for high-numerical-aperture optical systems[J]. Opt Lett 2003;28(10):801–3.
[21] Opstad I.S. 3DSIM data of mitochondria in the cardiomyoblast cell-line H9c2 adapted to either glucose or galactose[J]. Dataverse NO, V2,2021. Available from: https://doi.org/10.18710/PDCLAS
[22] Lal A, et al. Structured illumination microscopy image reconstruction algorithm[J]. IEEE J Sel Top Quantum Electron 2016;22(4):50–63.
[23] Křížek P, et al. SIMToolbox: a MATLAB toolbox for structured illumination fluorescence microscopy[J]. Bioinformatics 2016;32(2):318–20.
[24] Lei Y, et al. Multispectral scattering imaging based on metasurface diffuser and deep learning[J]. Phys Status Solidi Rapid Res Lett 2021;16(2):2100469.
[25] Li Y, et al. Deep-learning-enabled dual-frequency composite fringe projection profilometry for single-shot absolute 3D shape measurement[J]. Opto-Electron Adv 2022;5(5):210021.
[26] Anand V, et al. Single-shot mid-infrared incoherent holography using Lucy-Richardson-Rosen algorithm[J]. Opto-Electron Sci 2022;1(3) 210006-1-210006-8.
[27] Zanotto L, et al. Single-pixel terahertz imaging: a review[J]. Opto-Electron Adv 2020;3(9):09200012.